Theory and experiment of Fourier–Bessel field calculation and tuning of a pulsed wave annular array

Paul D Fox[a)]
Ørsted.DTU, Technical University of Denmark, Building 348, DK-2800 Lyngby, Denmark

Jiqi Cheng[b)] and Jian-yu Lu[c)]
Ultrasound Laboratory, Department of Bioengineering, University of Toledo, 2801 West Bancroft Street, Toledo, Ohio 43606-3390

(Received 1 June 2001; revised 1 October 2002; accepted 16 January 2003)

A one-dimensional (1D) Fourier–Bessel series method for computing and tuning (beamforming) the linear lossless field of flat pulsed wave annular arrays is developed and supported with both numerical simulation and experimental verification. The technique represents a new method for modeling and tuning the propagated field by linking the quantized surface pressure profile to a known set of limited diffraction Bessel beams propagating into the medium. This enables derivation of an analytic expression for the field at any point in space and time in terms of the transducer surface pressure profile. Tuning of the field then also follows by formulating a least-squares design for the transducer surface pressure with respect to a given desired field in space and time. Simulated and experimental results for both field computation and tuning are presented in the context of a 10-ring annular array operating at a central frequency of 2.5 MHz in water. © *2003 Acoustical Society of America.* [DOI: 10.1121/1.1560211]

PACS numbers: 43.20.Bi, 43.20.−f, 43.38.Hz [ANN]

I. INTRODUCTION

In this article we describe a method for computing and tuning linear lossless fields from flat pulsed wave (PW) annular arrays by using a one-dimensional (1D) Fourier–Bessel series.[1,2] The use of this series allows the propagated field to be described as a polychromatic set of nondiffracting J_0 Bessel beams[3,4] giving a linear mapping between the spatial quantization levels on the transducer surface and the propagated field at any point in space. The technique leads to a new method for both the tuning and fast computation of PW annular fields.

Bessel beams are the components of polychromatic X waves[5] and have been studied extensively in recent years.[5–13] Theoretically, nondiffracting beams such as Bessel beams and X waves can propagate superluminally (at a speed $c/\cos\zeta$ where c is the speed of sound and ζ is the Axicon angle[14,15]), to an infinite distance without spreading if they are produced with an infinite aperture and energy. In practice, nearly exact X waves can still be realized with either broadband or band-limited radiators over deep depth of field[5] and for this reason, these and other related beams[7,9,10,16–21] have been studied extensively for medical imaging,[22–24] tissue property identification,[25] blood flow velocity vector measurement,[26] nondestructive evaluation of materials,[27] communications,[28] electromagnetics,[29] and optics.[4,30]

The present study draws on previous knowledge of Bessel beams and X waves to formulate a method for both computing and tuning (beamforming) the propagated field by using a set of Bessel beam basis functions. In Refs. 31 and 32 these were applied across the transducer surface to decompose the emitted field into a known set of limited diffraction Bessel beams. In this article the analysis is extended to solve for the emitted field itself as a weighted set of exact Bessel solutions to the wave equation and study the method for polychromatic (pulsed) waves. We show that the method correlates well with both previous experimental results[6] and simulations based on the Rayleigh–Sommerfeld diffraction formula. The method also allows us to tune the PW field in a least-squares sense with respect to a given desired PW field distribution by choosing the transducer surface quantization levels accordingly.

In Sec. II model definitions for the governing wave equation and structure of PW annular arrays are introduced. Section III then explains the application and interpretation of 1D Fourier–Bessel series and Sec. IV develops a method for computing the propagated field using these series. Section V gives numerical examples of the field computation for X waves and focused Gaussian pulses, comparing them also to experimental data and a classical (Rayleigh–Sommerfeld) field calculation method. In Sec. VI a least-squares field tuning design is given, followed in Sec. VII by numerical examples for X waves and focused Gaussian pulses. Finally, Sec. VIII summarizes, draws conclusions, and suggests further work.

II. MODEL DEFINITIONS

A. Propagation model

Annular arrays have circular symmetry and correspondingly the resulting propagation in linear free space is dictated by the circular-symmetric wave equation

[a)]Electronic mail: pdf@oersted.dtu.dk
[b)]Electronic mail: jcheng@eng.utoledo.edu
[c)]Electronic mail: jilu@eng.utoledo.edu

 0001-4966/2003/113(5)/2412/12/$19.00

$$\left[\frac{1}{r}\frac{\partial}{\partial r}\left(r\frac{\partial}{\partial r}\right)+\frac{\partial^2}{\partial z^2}-\frac{1}{c^2}\frac{\partial^2}{\partial t^2}\right]f(r,z,t)=0, \tag{1}$$

where $f(r,z,t)$ is the scalar field value, r is the radial distance from the cylindrical centerline, z is the outward propagation distance perpendicular to the transducer surface (sitting in the $z=0$ plane and centered around $r=0$), and c is the speed of sound (assumed real). This equation has an infinite number of Bessel beam solutions[4,5] of the form

$$\begin{aligned} &f(r,z,t,\omega)=J_0(\alpha r)e^{j\beta z}e^{-j\omega t},\\ &\beta=\sqrt{k^2-\alpha^2}:\quad k=\omega/c, \end{aligned} \tag{2}$$

where k is the wave number (real) and α any real nonnegative value ($\alpha\geqslant 0$).

Notice that for $\alpha>k$, the axial parameter $\beta=\sqrt{k^2-\alpha^2}$ becomes imaginary and in this case $f(r,z,t,\omega)$ decays exponentially rapidly in the z direction. In particular, it becomes an evanescent wave for large enough β and this will become a key property in the development of the field calculation. The other important property is that at $z=0$ the field is $f(r,0,t,\omega)=J_0(\alpha r)\cdot e^{-j\omega t}$, and therefore a pressure profile $J_0(\alpha r)e^{-j\omega t}$ at $z=0$ necessarily gives rise to a propagating Bessel beam (2). Therefore, if it is possible to describe the field over an annular transducer's surface as a sum of terms of the type $f(r,0,t,\omega)=J_0(\alpha r)e^{-j\omega t}$ with different α and β values, the propagating field in linear media becomes the summation of each individual field given by Eq. (2). And since Eq. (2) is an equation not involving costly numerical computations such as integration, this approach demonstrates potential for fast field computation.

B. PW annular arrays

We consider flat annular N-ring PW arrays of radius R with surface pressure $q(r,t)$, which are quantized spatially in the radial r direction due to their ring structure. This results in N sequentially discretized pressure profiles $q_p(t)$, where $p=1,\ldots,N$ is the ring number and $p=1$ for the inner ring with $p=N$ for the outer ring. Time and frequency domain representations $q_p(t)$ and $Q_p(\omega)$ for each ring p are linked formally by the continuous Fourier transform pair

$$\begin{aligned} Q_p(\omega)&=\int_{-\infty}^{\infty}q_p(t)e^{j\omega t}dt\\ &\Leftrightarrow q_p(t)=\frac{1}{2\pi}\int_{-\infty}^{\infty}Q_p(\omega)e^{-j\omega t}d\omega, \end{aligned} \tag{3}$$

although we assume here a sampled system with fixed pulse repeat frequency such that the system is represented by the discrete Fourier sum

$$\begin{aligned} &q_p(t_d)=\sum_{s=0}^{n_\omega}Q_p(\omega_s)e^{-j\omega_s t_d}:\quad \omega_s=s2\pi f_0\\ &Q_p(\omega_s)=\mathrm{FFT}\{q_p(t_d)\}\Leftrightarrow q_p(t_d)=\mathrm{IFFT}\{Q_p(\omega_s)\}, \end{aligned} \tag{4}$$

where n_ω is the number of nonzero Fourier frequencies, f_0 denotes fundamental frequency in hertz, and t_d denotes a discrete sampling point in time. The notation $\mathrm{FFT}\{q_p(t_d)\}$ denotes taking the fast fourier transform (FFT) of $q_p(t)$ and $\mathrm{IFFT}\{Q_p(\omega_s)\}$ denotes the inverse fast fourier transform (IFFT) of $Q_p(\omega_s)$. Hence the entire array of all N rings may then be represented as

$$\begin{bmatrix} q_1(t_d)\\ \vdots\\ q_N(t_d)\end{bmatrix}=\sum_{s=0}^{n_\omega}\begin{bmatrix} Q_1(\omega_s)\\ \vdots\\ Q_N(\omega_s)\end{bmatrix}e^{-j\omega_s t_d} \tag{5}$$

in which each entry $Q_p(\omega_s)$ for $p=1,\ldots,N$ is generally complex

$$Q_p(\omega_s)=\gamma_p(\omega_s)+j\,\delta_p(\omega_s) \tag{6}$$

with $\gamma_p(\omega_s)$ and $\delta_p(\omega_s)$ being the real and imaginary parts of $Q_p(\omega_s)$, respectively. This corresponds to each ring emitting pressure $Q_p(\omega_s)e^{-j\omega_s t_d}=|Q_p(\omega_s)|e^{j\theta_p(\omega_s)}e^{-j\omega_s t_d}=|Q_p(\omega_s)|e^{-j\omega_s(t_d-\tau_p(\omega_s))}$, where $|Q_p(\omega_s)|$, $\theta_p(\omega_s)$, and $\tau_p(\omega_s)$ are the respective ring magnitudes, phases, and time delays obtained from Eq. (6) as

$$\begin{aligned} &|Q_p(\omega_s)|=\sqrt{\gamma_p(\omega_s)^2+\delta_p(\omega_s)^2},\\ &\theta_p(\omega_s)=-j\ln(Q_p(\omega_s)/|Q_p(\omega_s)|),\\ &\tau_p(\omega_s)=\theta_p(\omega_s)/\omega_s. \end{aligned} \tag{7}$$

III. USE OF 1D FOURIER–BESSEL SERIES

A. Application of infinite series

A 1D Fourier-Bessel series[1,2] may be used to model the quantized surface pressure $q(r,\omega_s)$ at each frequency ω_s in Eq. (4) by an infinite set of known basis Bessel functions as

$$\begin{aligned} &Q(r,\omega_s)=\sum_{i=1}^{\infty}A_i(\omega_s)J_0(\alpha_i r),\\ &\alpha_i=x_i/a:\quad J_0(x_i)=0,\\ &A_i(\omega_s)=\frac{2}{a^2J_1^2(x_i)}\int_0^a q(r,\omega_s)rJ_0(\alpha_i r)dr, \end{aligned} \tag{8}$$

where $J_0(\cdot)$ is the Bessel function of the first kind of order zero and x_i in Eq. (8) are the known infinite set of (real) monotonically increasing positive solutions to $J_0(x_i)=0$. This series applies over the range $0\leqslant r\leqslant a$ for any choice of modeling aperture a, subject to $Q(a,\omega_s)=0$ due to $J_0(\alpha_i a)=J_0(x_i)=0$ for all i. (Note also that for ease of discussion, we use the term *aperture* here to refer to the modeling radius a rather the full diameter $2a$.) For annular arrays, we may therefore select any value $a>R$ since the surface pressure $Q(r,\omega_s)$ is considered to be zero for $r\geqslant R$ in the transducer plane $z=0$.

The spatial profile $Q(r,\omega_s)$ for a given ω_s is stepwise constant $Q(r,\omega_s)=Q_p(\omega_s)$ for the N rings $p=1,\ldots,N$ present over the radial range $0\leqslant r\leqslant R$. Beyond this range it becomes $Q(r,\omega_s)=0$ for $R<r\leqslant a$ and together these two consecutive ranges allow $A_i(\omega_s)$ in Eq. (8) to be evaluated analytically as

$$\begin{aligned} &A_i(\omega_s)=\sum_{p=1}^{N}C_{i,p}Q_p(\omega_s),\\ &C_{i,p}=2[r_p^+J_1(\alpha_i r_p^+)-r_p^-J_1(\alpha_i r_p^-)]/ax_iJ_1^2(x_i), \end{aligned} \tag{9}$$

where $J_1(\cdot)$ is the first-order Bessel function of the first kind and r_p^-, r_p^+ are inner and outer radii of ring p, respectively. [Hence $r_1^-=0$ (transducer center) and $r_N^+=R$ (transducer outer edge) by definition, with the kerf between successive rings being $r_p^- - r_{p-1}^+$ for $p=2,\ldots,N$.] Note also that the quantities $A_i(\omega_s)$ are complex since $Q_p(\omega_s)$ in Eqs. (4)–(6) are complex and only $C_{i,p}$ in Eq. (9) are real. See Ref. 13 for a more detailed numerical insight from the equivalent terms in the cw case.

Returning then to Eq. (8), the result is that the annular transducer pressure has now become equivalent to the infinite sum of weighted Bessel functions $Q(r,\omega_s)$. Hence, when multiplied through by their common temporal component $e^{-j\omega_s t}$, the transducer pressure becomes $Q(r,\omega_s)e^{-j\omega_s t}=\Sigma_{i=1}^{\infty}A_i(\omega_s)J_0(\alpha_i r)e^{-j\omega_s t}$ in which each weighted component $J_0(\alpha_i r)e^{-j\omega_s t}$ is a Bessel beam solution (2) to the wave equation (1) at $z=0$. Correspondingly, an infinite set of known Bessel beams propagate into the medium as

$$f(r,z,t,\omega_s)=\sum_{i=1}^{\infty}A_i(\omega_s)J_0(\alpha_i r)\cdot e^{j\beta_i(\omega_s)z}e^{-j\omega_s t},$$
$$\beta_i(\omega_s)=\sqrt{k_s^2-\alpha_i^2}:\quad k_s=\omega_s/c, \tag{10}$$

where $A_i(\omega_s)\cdot J_0(\alpha_i r)e^{j\beta_i(\omega_s)z}e^{-j\omega_s t}$ is the full Bessel solution for $z\neq 0$ to Eq. (1), $k_s=\omega_s/c$ is the wave number, and α_i, $\beta_i(\omega_s)$ are the propagation parameters in the radial and axial directions r, z, respectively.

B. Truncation to finite series

Now consider the behavior of $\beta_i(\omega_s)$ in Eq. (10) as the coefficient index i changes. The scaling parameters $\alpha_i=x_i/a$ in Eq. (8) increase monotonically with index i for a given value of a since the roots $x_i\approx\pi i-\pi/4$ increase monotonically with i by definition. Hence a change in propagation characteristics occurs for the distinct cases $\alpha_i\leqslant k_s$ and $\alpha_i>k_s$ since the wave number k_s is real and hence $\beta_i(\omega_s)$ is purely real when $\alpha_i\leqslant k_s$ but purely imaginary when $\alpha_i>k_s$. For the case of real $\beta_i(\omega_s)$, all the corresponding components in Eq. (10) propagate to infinity due to $|e^{j\beta_i(\omega_s)z}|=1$ even as $z\to\infty$. However, for the case of imaginary $\beta_i(\omega_s)$, the corresponding components usually all become evanescent since $e^{-|\beta_i(\omega_s)|z}\ll 1$ even for very small values of z in typical ultrasonic applications. Notice also from the definition of $\beta_i(\omega_s)$ in Eq. (10) that the evanescent terms $e^{-|\beta_i(\omega_s)|z}$ decay more and more rapidly with respect to z as i increases since $|\beta_i(\omega_s)|$ increases monotonically with i for all values $\alpha_i>k_s$. This means that even if a certain number of $\alpha_i>k_s$ terms are retained for a given application, all higher terms in the series may always be neglected by definition. (See Ref. 13 for a more detailed numerical discussion in the cw case.) Therefore only the nonevanescent beam components are considered for most practical purposes, and denoting $l(k_s,a)$ as the appropriate number of nonnegligible components for a given application, the infinite sum in Eq. (10) becomes replaced by the finite limited diffraction sum

$$f(r,z,t,\omega_s)=\sum_{i=1}^{l(k_s,a)}A_i(\omega_s)J_0(\alpha_i r)e^{j\beta_i(\omega_s)z}e^{-j\omega_s t}. \tag{11}$$

This truncation limit $l(k_s,a)$ may also be estimated analytically by replacing k with k_s in the expression for $l(k,a)$ derived previously in Refs. 13 and 32 to obtain

$$l(k_s,a)\approx k_s a/\pi+1/4, \tag{12}$$

which is proportional to wave number k_s and modeling aperture a, but independent of any particular transducer pressure $Q(r,\omega_s)$.

IV. THEORY FOR FIELD COMPUTATION

A. Field computation theory based on Fourier–Bessel series

When implemented over an infinite aperture ($a\to\infty$), the entire transducer plane at $z=0$ from $r=0$ to $r=\infty$ at $z=0$ becomes modeled by the Fourier–Bessel series. Then the propagating field at time t_d is given by the infinite aperture implementation of Eq. (11), namely

$$f(r,z,t_d,\omega_s)=F(r,z,\omega_s)e^{-j\omega_s t_d},$$
$$F(r,z,\omega_s)=\lim_{a\to\infty}\sum_{i=1}^{l(k_s,a)}J_0\left(\frac{x_i r}{a}\right)e^{j\beta_i(\omega_s)z}\times\left[\sum_{p=1}^{N}C_{i,p}(\gamma_p(\omega_s)+j\,\delta_p(\omega_s))\right], \tag{13}$$

and the complex terms $F(r,z,\omega_s)$ are obtained from Eqs. (11), (9), and (6). Notice from Eq. (13) that the terms $F(r,z,\omega_s)$ are Fourier coefficients mapping the transducer surface pressures $Q_p(\omega_s)=\gamma_p(\omega_s)+j\,\delta_p(\omega_s)$ to the field $f(r,z,t_d,\omega_s)$ at arbitrary positions r, z. Hence defining the total field $f(r,z,t_d)$ as the sum $\Sigma_{s=0}^{n_\omega}f(r,z,t_d,\omega_s)$ of all subfields $f(r,z,t_d,\omega_s)$ in Eq. (13) gives

$$f(r,z,t_d)=\sum_{s=0}^{n_\omega}F(r,z,\omega_s)e^{-j\omega_s t_d}$$
$$\Rightarrow f(r,z,t_d)=\mathrm{IFFT}\{F(r,z,\omega_s)\}, \tag{14}$$

which is to say that the field $f(r,z,t_d)$ may now, in principle, be evaluated rapidly as an IFFT operation for any point in space and from any set of transducer surface pressures $Q_p(\omega_s)$.

However, a numerical problem appears at this point with regard to implementation. Equation (12) indicates $l(k_s,a)\to\infty$ as $a\to\infty$, and hence an infinite number of terms need to be summed in Eq. (13) to evaluate $F(r,z,\omega_s)$. This occurs as the difference $\alpha_i-\alpha_{i-1}\approx\pi/a$ between successive α_i values in Eq. (8) decreases as a increases, and hence more and more α_i terms appear in the nonevanescent range $0\leqslant\alpha_i\leqslant k_s$ as a increases. Clearly it is impossible to compute an infinite number of terms in practice, but the following scheme may be implemented to circumvent the problem. First replace the infinite limit $a\to\infty$ in Eq. (13) with a smaller fixed value of a, such as $a=10R$. Obtain an estimate of $F(r,z,\omega_s)$ from Eq. (13) based on $a=10R$ and then increase a to $a=15R$. Obtain a revised estimate of $F(r,z,\omega_s)$ based on $a=15R$ and

compare it to the estimate obtained for $a=10R$. If significantly different, increase a to $a=20R$ and compare estimates for $a=20R$ with $a=15R$. Continue to increase a until estimates for $F(r,z,\omega_s)$ based on successive values of a effectively converge to constant values. Take the converged estimate of $F(r,z,\omega_s)$ as the final practical approximation to the limiting case $a\to\infty$ and use this value for insertion into the IFFT operation of Eq. (14). See Ref. 13 for a detailed illustration of this convergence method at a given propagation frequency.

In practice we have found that convergence typically occurs at relatively modest values of a, such as $a=20R$. Therefore $a=10R$, $a=15R$, $a=20R$ has been adopted as the default convergence test sequence for the numerical examples given later in this paper. The convergence test itself was defined as the value of a for which the change in magnitude $|F(r,z,\omega_s)|$ between latest and previous value of a dropped to within 0.1% of the magnitude $|F(r,z,\omega_s)|$ for the previous value of a. The field calculation results obtained then proved both fast and accurate when compared against the Rayleigh–Sommerfeld field calculation technique. (See Sec. V for examples and discussion.)

B. Algorithm for field calculation

The field calculation algorithm resulting from Secs. II–IV may now be summarized as follows:

(1) If not known a priori, obtain the Fourier coefficients $Q_p(\omega_s)=\mathrm{FFT}\{q_p(t_d)\}$ for $p=1,...,N$ from Eq. (4).
(2) Set frequency index to $s=0$.
(3) Select initial modeling aperture a (e.g., $a=10R$, $a=15R$, $a=20R$, etc.).
(4) Estimate the corresponding number of nonevanescent terms $l(k_s,a)$ from Eq. (12).
(5) Evaluate coefficients $C_{i,p}$ for $i=1,\ldots,l(k_s,a)$ from Eq. (9).
(6) Evaluate $F(r,z,\omega_s)$ based on Eq. (13) but with the infinite limit $a\to\infty$ removed.
(7) Increase i beyond $i=l(k_s,a)$ to ensure that evanescence occurs for z regions of interest when $\alpha_i>k$ [i.e., check for any significant changes in $F(r,z,\omega_s)$]. Stop increasing i when no significant changes are detected.
(8) Compare current evaluation of $F(r,z,\omega_s)$ with that for previous value of a. If not converged to within satisfactory limit, increase the value of a and go back to step (4).
(9) If $s<n_\omega$, increase s by 1 and go back to step (3).
(10) Evaluate the field as $f(r,z,t_d)=\mathrm{IFFT}\{F(r,z,\omega_s)\}$ from Eq. (14) based on all coefficients $F(r,z,\omega_s)$.

V. EXAMPLES OF FIELD COMPUTATION

A. Transducer geometry and simulated transducer data

For numerical examples of both field computation in this section and tuning in Sec. VII, we consider the PZT ceramic/polymer composite J_0 Bessel transducer of Lu and Greenleaf described in Ref. 6. The experimental setup for the experiment results quoted later in this paper are also described therein. The transducer is an $N=10$-ring Bessel design transducer whose ring edges are located nominally at the first 10 zeros of $J_0(\alpha r)$, where $\alpha=1202.45\ \mathrm{m}^{-1}$. In practice this transducer also has a kerf of approximately 0.2 mm, such that in terms of the notation of Sec. II B, $r_1^-=0$, $r_1^+=x_1/\alpha-\mathrm{kerf}/2$, $r_2^-=x_1/\alpha+\mathrm{kerf}/2$, and so on. The outer radius is also truncated from the nominal $R=25.48$ mm to $R=25$ mm in practice, and operating conditions are a central frequency of $f_c=2.5$ MHz ($\omega_c=15.71\ \mathrm{Mrad\,s}^{-1}$) in water at speed of sound $c=1500\ \mathrm{m\,s}^{-1}$ giving central wave number $k_c=10{,}471.98\ \mathrm{m}^{-1}$. In addition, the transfer function of the transducer is modeled as a Blackman window $B(\omega_s)$:

$$\begin{aligned} B(\omega_s)&=0.42-0.5\cos(\pi\omega_s/\omega_c)\\ &\quad+0.08\cos(2\pi\omega_s/\omega_c):\quad 0\leqslant\omega_s\leqslant 2\omega_c,\\ B(\omega_s)&=0:\quad \omega_s>2\omega_c, \end{aligned} \tag{15}$$

which exhibits zero phase shift for all ω_s, with $B(0)=0$ and $B(\omega_s)$ peaking at the central frequency $f_c=2.5$ MHz and possessing a -6 dB bandwidth of approximately $0.81f_c$. See Ref. 6 for further discussion of experimental setup and transducer characteristics. For PW studies, we assume a temporal excitation burst weighting function $g(t)$ given by

$$g(t_d)=e^{-t_d^2/t_0^2}\sin(2\pi f_c t_d), \tag{16}$$

where $t_0=0.4\ \mu$s, the burst lasts approximately one and a half cycles, and the total observation time is 20.48 μs. This gives fundamental frequency $f_0=1/20.48\ \mu\mathrm{s}=48.828$ kHz and with a maximum propagated frequency of 5 MHz due to Eq. (15), the Shannon sampling frequency is 10 MHz. In practice we implement a 100 MHz sampling rate, corresponding to sampling interval of 0.01 μs and a total number of $2048=2^{11}$ samples ($n_\omega=1024-1$ frequencies) for the FFT and IFFT operations. The excitation burst weighting $g(t_d)$ is then represented by the equivalent Fourier sum

$$g(t_d)=\sum_{s=0}^{n_\omega} G(\omega_s)e^{-j\omega_s t_d}\Rightarrow G(\omega_s)=\mathrm{FFT}\{g(t_d)\}. \tag{17}$$

Finally we define also the underlying driving function $x_p(t_d)$ similarly as

$$x_p(t_d)=\sum_{s=0}^{n_\omega} X_p(\omega_s)e^{-j\omega_s t_d}\Rightarrow X_p(\omega_s)=\mathrm{FFT}\{x_p(t_d)\}, \tag{18}$$

where $x_p(t_d)$ represents the user-defined driving function for each ring p: in our case we shall be considering X waves and focused Gaussian beams as these driving functions. Linking together $X_p(\omega_s)$, $G(\omega_s)$, and $B(\omega_s)$ in series from Eqs. (18), (17), and (15) then gives the final transmission quantization values $Q_p(\omega_s)$ and $q_p(t)$ as

$$\begin{aligned} Q_p(\omega_s)&=X_p(\omega_s)G(\omega_s)B(\omega_s)\\ &\Rightarrow q_p(t)=\mathrm{IFFT}\{X_p(\omega_s)G(\omega_s)B(\omega_s)\}, \end{aligned} \tag{19}$$

which allows the generation of either $Q_p(\omega_s)$ or $q_p(t_d)$ in Eq. (4) corresponding to any desired driving function $x_p(t_d)$. In the remainder of this section we compare the results of the Fourier–Bessel field calculation with both the Rayleigh–

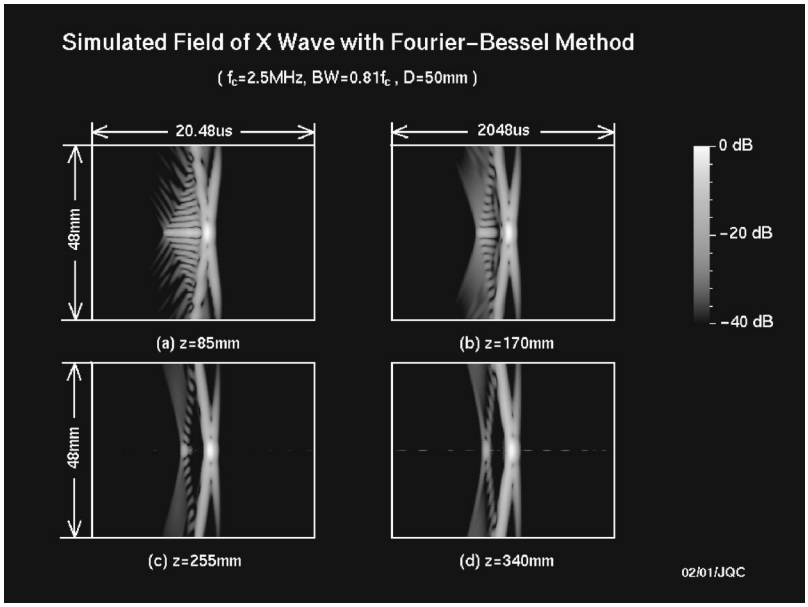

FIG. 1. Simulated fields of a zero-order band-limited X wave with Fourier–Bessel method at distances: (a) $z=85$ mm, (b) $z=170$ mm, (c) $z=255$ mm, and (d) $z=340$ mm, respectively, away from the surface of a 50-mm-diam annular array. A stepwise X wave aperture weighting and a broadband pulse drive of the array were assumed. The transmitting transfer function of the array was assumed to be the Blackman window function peaked at 2.5 MHz and with -6 dB bandwidth around $0.81f_c$. Parameters a_0 and ζ are 0.05 mm and 4°, respectively.

Sommerfeld field calculation and the experimentally measured field given in Ref. 33 for both X waves and focused Gaussian pulses. In Sec. VII we demonstrate tuning of these two types of fields with the same transducer.

B. Simulated and experimental field results

For the purposes of generating simulation data, we take $q_p(t_d)=\mathrm{IFFT}\{X_p(\omega_s)G(\omega_s)B(\omega_s)\}$ in Eq. (19) as the starting points from which to apply both the Fourier–Bessel (FB) field calculation algorithm of Sec. IV B and, for comparison/verification purposes, the more classical Rayleigh–Sommerfeld (RS) field calculation method. The driving function $x_p(t_d)$ for a (zero order) X wave[5,6] at $z=0$ on the transducer surface has frequency domain representation

$$X_p(\omega_s)=(2\pi a_0/c)e^{-a_0\omega_s/c}J_0(r_p\omega_s/c\,\sin\zeta), \tag{20}$$

where $a_0=0.05$ mm, $\zeta=4°$, $r_1=0$, $r_p=(r_p^-+r_p^+)/2$, $(p=2\cdots10)$ and $c=1500\ \mathrm{ms}^{-1}$. The focused Gaussian beam driving function $x_p(t_d)$ has frequency domain representation

$$X_p(\omega_s)=e^{-r_p^2/\sigma^2}e^{j\cdot\omega_s/c\cdot(F-\sqrt{F^2+r_p^2})}, \tag{21}$$

where $\sigma=15$ mm and the focus F is located at $F=120$ mm, with the full-width-at-half-maximum being 25 mm.

1. X wave field

Figure 1 shows the FB calculated field of a simulated X wave, where $X_p(\omega_s)$ is defined as per Eq. (20). The FB algorithm converged for all values at $a=20R$ and the field is shown at the four distances, (a) $z=85$ mm, (b) $z=170$ mm, (c) $z=255$ mm, (d) $z=340$ mm. In all four panels, the horizontal axis represents time whilst the vertical axis represents the radial position away from the center of the transducer. Figure 2 then shows the RS field calculation of the same simulated X wave as per Fig. 1. The FB and RS plots are virtually identical, and this parallel is offered as an

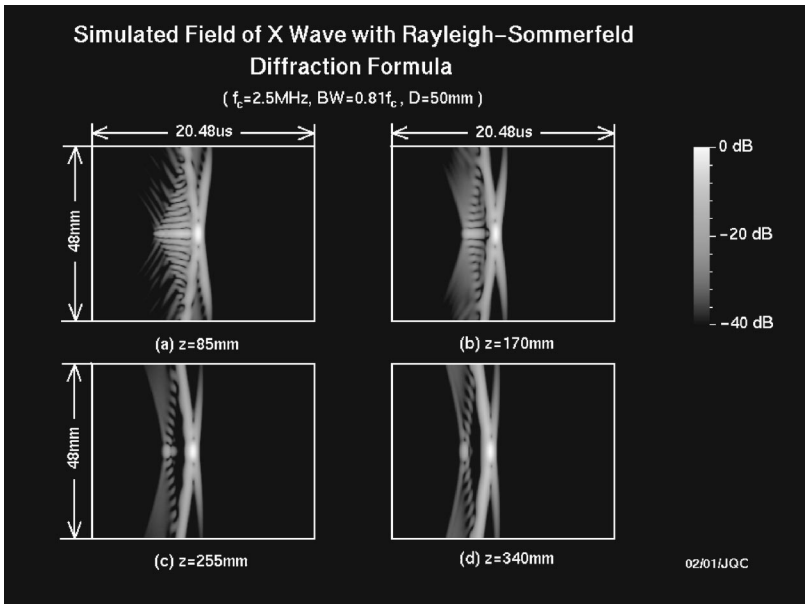

FIG. 2. The images are the same as those in Fig. 1, except that they are produced with the Rayleigh–Sommerfeld diffraction formula. The layout and the parameters used in simulation are the same as those in Fig. 1.

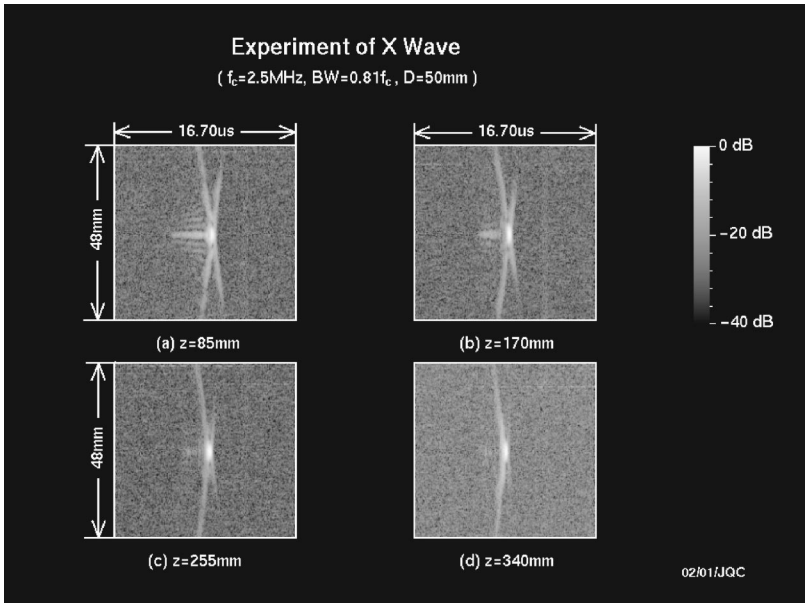

FIG. 3. Experimental results that correspond to the simulations in Figs. 1 and 2. A 10-element, 50-mm diameter, 2.5MHz central frequency, PZT ceramic/polymer composite J_0 Bessel transducer was used.

indicator of the F-B algorithm's accuracy since the R-S algorithm is widely accepted as a reliable method for field calculation. Figure 3 shows actual experimental results for the Bessel transducer of Ref. 6, which match the predicted simulated X wave fields given previously in Figs. 1 and 2. See Ref. 33 for details of experimental setup. A high level of agreement between theory and practice is observed. Notice also that the FB algorithm is applicable right up to and including the transducer surface itself since Eq. (13) applies for all $z \geqslant 0$, whereas the RS algorithm is not applicable close to the transducer surface.

When programmed in C under Linux on a Pentium III 600 MHz PC with 128 M Bytes of RAM, the FB algorithm took approximately 1 min and the RS algorithm approximately 10 h. However, a study of runtimes compared with faster computational techniques such as the impulse response method[34–39] has not yet been conducted at this point in time.

2. Gaussian field

Figure 4 shows FB field calculation for the simulated focused Gaussian pulse, where $X_p(\omega_s)$ is given by Eq. (21) and plots are shown for (a) $z=50$ mm, (b) $z=120$ mm, (c) $z=150$ mm, (d) $z=216$ mm. Figure 5 then gives the RS field calculation for the same pulse, again showing a close correlation between the FB and RS simulation methods. Finally, Fig. 6 shows experimental results except that in the experimental test of Ref. 6 the transducer had an acoustic lens added. This supplied a continuous phase shift across the transducer surface rather than the discretized phase shifts assumed in the simulation. Therefore some differences between Fig. 6 and Figs. 4 and 5 are expected. This is evidenced in the differences observed for the near field and far field panels (a) and (d) between the respective figures, al-

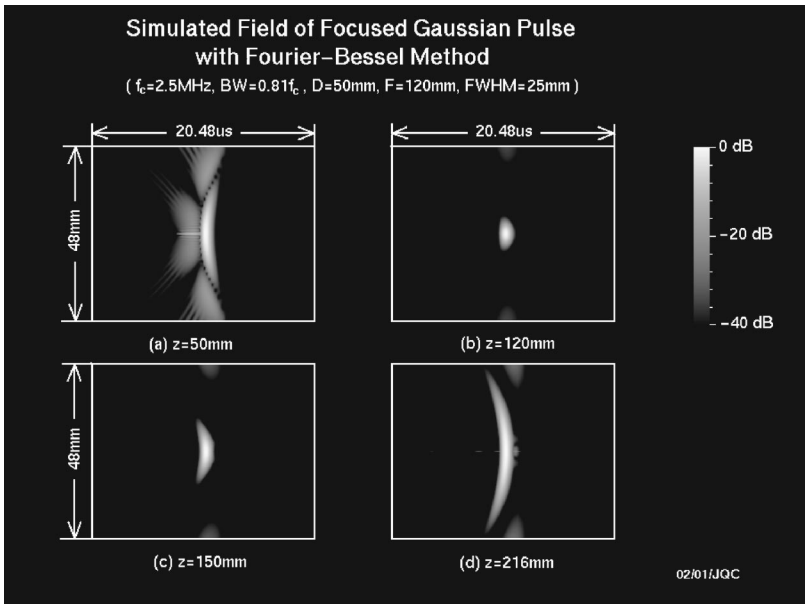

FIG. 4. Simulated fields of a focused Gaussian pulse with Fourier–Bessel method at distances: (a) $z=50$ mm, (b) $z=120$ mm, (c) $z=150$ mm, and (d) $z=216$ mm. A stepwise Gaussian aperture shading and a stepwise phase was assumed. The broadband pulse and transmitting transfer function of the array are the same as those for the X wave in Fig. 1. The FWHM of the Gaussian shading was 25 mm.

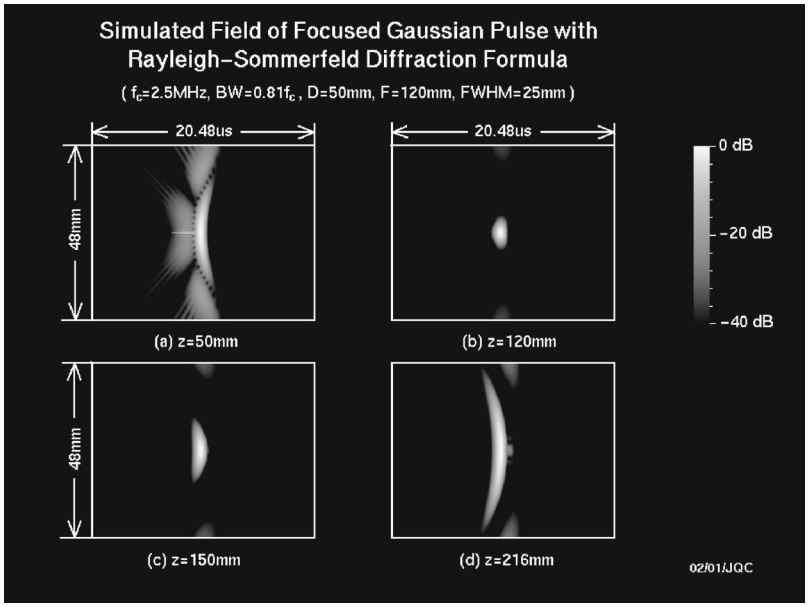

FIG. 5. The images are the same as those in Fig. 4, except that they are produced with the Rayleigh–Sommerfeld diffraction formula. The layout and the parameters used in simulation are the same as those in Fig. 4.

though the simulated and experimental pulses are very similar in the closer regions around the focus in panels (b) and (c), respectively.

VI. THEORY FOR TUNING

A. Tuning theory-based on Fourier–Bessel series

We consider now how to tune the transducer surface pressure in order to produce (as closely as physically possible) a particular desired propagating field. Assuming a given desired field $d(r,z,t_d)$ in the form

$$d(r,z,t_d)=\sum_{s=0}^{n_\omega} D(r,z,\omega_s)e^{-j\omega_s t_d}$$

$$\Rightarrow D(r,z,\omega_s)=\mathrm{FFT}\{d(r,z,t_d)\} \tag{22}$$

the tuning technique adopted will be to consider each frequency component $d(r,z,t_d,\omega_s)=D(r,z,\omega_s)\cdot e^{-j\omega_s t_d}$ of the *desired* field separately, and to minimize the sum of squared differences between it and the corresponding *physically obtainable* field term $f(r,z,t_d,\omega_s)=F(r,z,\omega_s)\cdot e^{-j\omega_s t_d}$ in Eq. (13) over a given set of field points r, z of interest. Due to the common time element $e^{-j\omega_s t_d}$ in both terms, this problem reduces to minimizing the squared sums of the Fourier coefficient differences $S(\omega_s)=\Sigma_{r,z}\|F(r,z,\omega_s)-D(r,z,\omega_s)\|^2$. Separating out $F(r,z,\omega_s)$ and $D(r,z,\omega_s)$ into real and imaginary parts then gives

$$F(r,z,\omega_s)=F^{\Re}(r,z,\omega_s)+jF^{\Im}(r,z,\omega_s),$$

$$D(r,z,\omega_s)=D^{\Re}(r,z,\omega_s)+jD^{\Im}(r,z,\omega_s), \tag{23}$$

$$S(\omega_s)=\sum_{r,z}\ ([F^{\Re}(r,z,\omega_s)-D^{\Re}(r,z,\omega_s)]^2$$

$$+[F^{\Im}(r,z,\omega_s)-D^{\Im}(r,z,\omega_s)]^2),$$

where $D(r,z,\omega_s)=\mathrm{FFT}\{d(r,z,t)\}$ from Eq. (22). Now, the

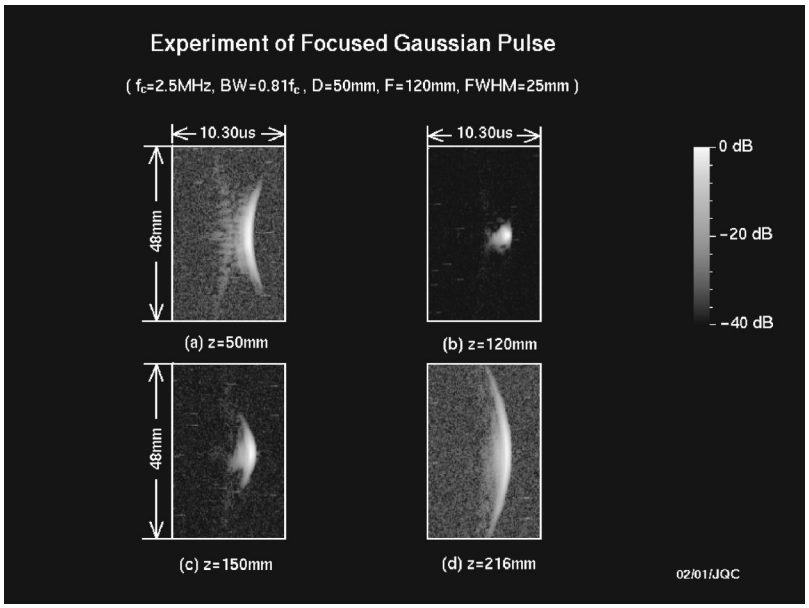

FIG. 6. Experimental results that correspond to the simulations in Figs. 4 and 5, except that in the experiment the phases applied by a lens was continuous. The same transducer for Fig. 3 was used.

obtainable field terms $F(r,z,\omega_s)$ in Eq. (13) are functions of the quantization levels $Q_1(\omega_s)\cdots Q_N(\omega_s)$ by definition, and so minimization of $S(\omega_s)$ necessarily requires adjustment of all their components $\gamma_p(\omega_s)$ and $\delta_p(\omega_s)$ as defined in Eq. (6). Then from Eqs. (13) and (6) the real and imaginary parts of $F(r,z,\omega_s)$ at all points of interest $r=r_u$, $z=z_v$ over a set of n_u radial indices $u=1\cdots n_u$ and n_v propagation indices $v=1\cdots n_v$ may then be written out as

$$\begin{bmatrix} F^{\Re}(r_1,z_1,\omega_s) \\ F^{\Im}(r_1,z_1,\omega_s) \\ \vdots \\ F^{\Re}(r_u,z_v,\omega_s) \\ F^{\Im}(r_u,z_v,\omega_s) \\ \vdots \\ F^{\Re}(r_{n_u},z_{n_v},\omega_s) \\ F^{\Im}(r_{n_u},z_{n_v},\omega_s) \end{bmatrix} = \begin{bmatrix} \lim\limits_{a\to\infty}\sum\limits_{i=1}^{l(k_s,a)} J_0\left(\frac{x_i r_1}{a}\right)\begin{bmatrix} +M^{\Re}_{i,1,1,s}, -M^{\Im}_{i,1,1,s},\ldots,+M^{\Re}_{i,N,1,s}, -M^{\Im}_{i,N,1,s} \\ +M^{\Im}_{i,1,1,s}, +M^{\Re}_{i,1,1,s},\ldots,+M^{\Im}_{i,N,1,s}, +M^{\Re}_{i,N,1,s}\end{bmatrix} \\ \vdots \\ \lim\limits_{a\to\infty}\sum\limits_{i=1}^{l(k_s,a)} J_0\left(\frac{x_i r_u}{a}\right)\begin{bmatrix} +M^{\Re}_{i,1,v,s}, -M^{\Im}_{i,1,v,s},\ldots,+M^{\Re}_{i,N,v,s}, -M^{\Im}_{i,N,v,s} \\ +M^{\Im}_{i,1,v,s}, +M^{\Re}_{i,1,v,s},\ldots,+M^{\Im}_{i,N,v,s}, +M^{\Re}_{i,N,v,s}\end{bmatrix} \\ \vdots \\ \lim\limits_{a\to\infty}\sum\limits_{i=1}^{l(k_s,a)} J_0\left(\frac{x_i r_{n_u}}{a}\right)\begin{bmatrix} +M^{\Re}_{i,1,n_v,s}, -M^{\Im}_{i,1,n_v,s},\ldots,+M^{\Re}_{i,N,n_v,s}, -M^{\Im}_{i,N,n_v,s} \\ +M^{\Im}_{i,1,n_v,s}, +M^{\Re}_{i,1,n_v,s},\ldots,+M^{\Im}_{i,N,n_v,s}, +M^{\Re}_{i,N,n_v,s}\end{bmatrix} \end{bmatrix} \begin{bmatrix} \gamma_1(\omega_s) \\ \delta_1(\omega_s) \\ \vdots \\ \gamma_N(\omega_s) \\ \delta_N(\omega_s) \end{bmatrix}, \tag{24}$$

where $M^{\Re}_{i,p,v,s}$ and $M^{\Im}_{i,p,v,s}$ are the real and imaginary parts of $C_{i,p}e^{j\beta_i(\omega_s)z_v}$, respectively ($p=1\cdots N$). This expression takes the block form

$$F(\omega_s)=M(\omega_s)T(\omega_s), \tag{25}$$

where

$$F(\omega_s)=[F^{\Re}(r_1,z_1,\omega_s),F^{\Im}(r_1,z_1,\omega_s),\ldots,F^{\Re}(r_{n_u},z_{n_v},\omega_s), F^{\Im}(r_{n_u},z_{n_v},\omega_s)]' \tag{26}$$

is the vector on the left-hand side of Eq. (24), with dimension $F(\omega_s)=\{2n_un_v,1\}$ in which the notation {*rows, columns*} indicates the numbers of *rows* and *columns*, respectively. The vector $T(\omega_s)$ is

$$T(\omega_s)=[\gamma_1(\omega_s),\delta_1(\omega_s),\ldots,\gamma_N(\omega_s),\delta_N(\omega_s)]' \tag{27}$$

appearing on the far right-hand side of Eq. (24) with dimension $T(\omega_s)=\{2N,1\}$. Finally $M(\omega_s)=\{2n_un_v,2N\}$ represents the limit as $a\to\infty$ of the large remaining matrix in Eq. (24) premultiplying $T(\omega_s)$. Similarly to $F(\omega_s)=\{2n_un_v,1\}$ in Eq. (26) we may then also define a vector $D(\omega_s)=\{2n_un_v,1\}$ as

$$D(\omega_s)=[D^{\Re}(r_1,z_1,\omega_s),D^{\Im}(r_1,z_1,\omega_s),\ldots,D^{\Re}(r_{n_u},z_{n_v},\omega_s), D^{\Im}(r_{n_u},z_{n_v},\omega_s)]', \tag{28}$$

which allows the error sum $S(\omega_s)$ in Eq. (23) to be written $S(\omega_s)=[F(\omega_s)-D(\omega_s)]'\cdot[F(\omega_s)-D(\omega_s)]$. Substituting for $F(\omega_s)=M(\omega_s)T(\omega_s)$ from Eq. (25) then gives $S(\omega_s)=[M(\omega_s)T(\omega_s)-D(\omega_s)]'[M(\omega_s)T(\omega_s)-D(\omega_s)]$ which may be minimized by adjusting all $p=1,\ldots,N$ components $\gamma_p(\omega_s)$, $\delta_p(\omega_s)$, in $T(\omega_s)$ appropriately. This is a standard linear least-squares problem with solution $T(\omega_s)=T_{ls}(\omega_s)$ given by

$$T_{ls}(\omega_s)=[M'(\omega_s)M(\omega_s)]^{-1}M'(\omega_s)D(\omega_s), \tag{29}$$

where $[M'(\omega_s)M(\omega_s)]^{-1}M'(\omega_s)$ is the Moore–Penrose pseudoinverse of $M(\omega_s)$. The existence of this pseudoinverse requires $[M'(\omega_s)M(\omega_s)]$ to be invertible, which is to say $[M'(\omega_s)M(\omega_s)]=\{2N,2N\}$ must have full rank $2N$; and since the rank of any matrix cannot exceed its lowest dimension, this cannot be achieved if the row dimension $2n_un_v$ of $M(\omega_s)=\{2n_un_v,2N\}$ is less than its column dimension $2N$. Hence we obtain the fundamental requirement $n_un_v\geqslant N$ in order to prevent $M(\omega_s)$ and thereby $M'(\omega_s)M(\omega_s)$ from being rank deficient for dimensional reasons. Assuming then that $M(\omega_s)$ is full rank for a given value of a, we also still need in practice to iterate increasing values of a to simulate $a\to\infty$ for the same reasons, as already discussed in Sec. IV A. In this case however, we calculate $T_{ls}(\omega_s)$ for each value of a and wait for the corresponding magnitudes $|T_{ls}(\omega_s)|$ to converge to within acceptable levels rather than to wait for $|F(r,z,\omega_s)|$ to converge as was the case in Sec. IV A. (See Ref. 13 for an illustration of quantization level convergence in the cw case).

In addition, consideration also needs to be given to the spatial sampling rates in the given region of interest. From Eq. (11) we observe that the nonevanescent components i of the sum propagate in the z direction as $e^{j\beta_i(\omega_s)z}$ with wavelength $2\pi/\beta_i(\omega_s)$. The shortest possible wavelength is therefore that corresponding to the maximum possible nonevanescent value of $\beta_i(\omega_s)$, namely $\beta_{\max}=k_s$ which occurs when $\alpha_i=0$ in Eq. (10). This gives a wavelength of $2\pi/k_s$, and to comply with the Shannon sampling theorem this dictates a corresponding sampling interval in the z direction of π/k_s or lower. With respect to the radial direction r, the approximation $J_0(\alpha_i r)\approx\sqrt{2/\pi\alpha_i r}\cos(\alpha_i r-\pi/4)$ from Refs. 1 and 2 allows us to approximate the radial oscillations as a cosine function of wavelength $2\pi/\alpha_i$. The minimum wavelength possible is therefore also $2\pi/k_s$, corresponding to the maximum nonevanescent value $\alpha_i=k_s$ possible in Eq. (10). This gives maximum sampling interval in the r direction also of π/k_s. Finally, considering that the highest wave number present in the system is k_{n_ω} corresponding to $s=n_\omega$, we adopt a final maximum sampling interval of $\pi/k_{n_\omega}=\pi/2k_c$

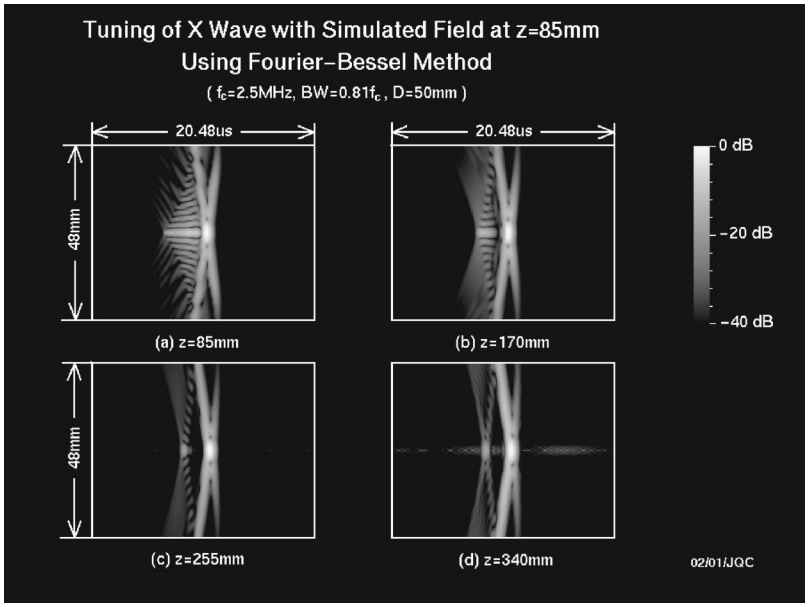

FIG. 7. Tuning results of X wave with simulated field at $z=85$ mm [Fig. 1(a)] as a desired field using Fourier–Bessel method. With the tuned weighting of the transducer, fields were reconstructed at distances: (a) $z=85$ mm, (b) $z=170$ mm, (c) $z=255$ mm, and (d) $z=340$ mm, respectively, away from the transducer surface.

$=c/2f_0n_\omega$ m in both r and z directions in order to cover the highest spatial oscillations present in the system.

B. Algorithm for tuning

From the discussion in Sec. VI A and including knowledge already gained in Secs. II–IV, the tuning algorithm becomes the following.

(1) If not known a priori, obtain Fourier coefficients $D(r,z,\omega_s)=\mathrm{FFT}\{d(r,z,t_d)\}$ from Eq. (22) for desired field. Make sure that $D(r,z,\omega_s)$ is specified at all points of interest $r=r_u$, $z=z_v$ $(u=1\cdots n_u$ and $v=1\cdots n_v)$, with sampling interval in both r and z directions being at most $\pi/k_{n_\omega}=\pi/2k_c=c/2f_0n_\omega$ m.
(2) Set frequency index to $s=0$.
(3) Select initial modeling aperture a (e.g., $a=10R$, $a=15R$, $a=20R$, etc.).
(4) Estimate the corresponding number of nonevanescent terms $l(k_s,a)$ from Eq. (12).
(5) Evaluate coefficients $C_{i,p}$ for $i=1,\ldots,l(k_s,a)$ from Eq. (9).
(6) Evaluate $M(\omega_s)$ based on Eq. (24) but with the infinite limit $a\to\infty$ removed.
(7) If necessary, continue to increase i until $\alpha_i>k$ to ensure numerically that the evanescence limit has been reached. If any of the first few evanescent terms still contribute significantly in the ranges of z of interest, include them in the sum for $M(\omega_s)$. Stop increasing i when no further terms are significant.
(8) Evaluate least-squares quantization vector $T_{ls}(\omega_s)$ from Eq. (29).
(9) Compare current evaluation of $T_{ls}(\omega_s)$ with that for previous value of a. If not converged to within satisfactory limit, increase the value of a and go back to step (4).

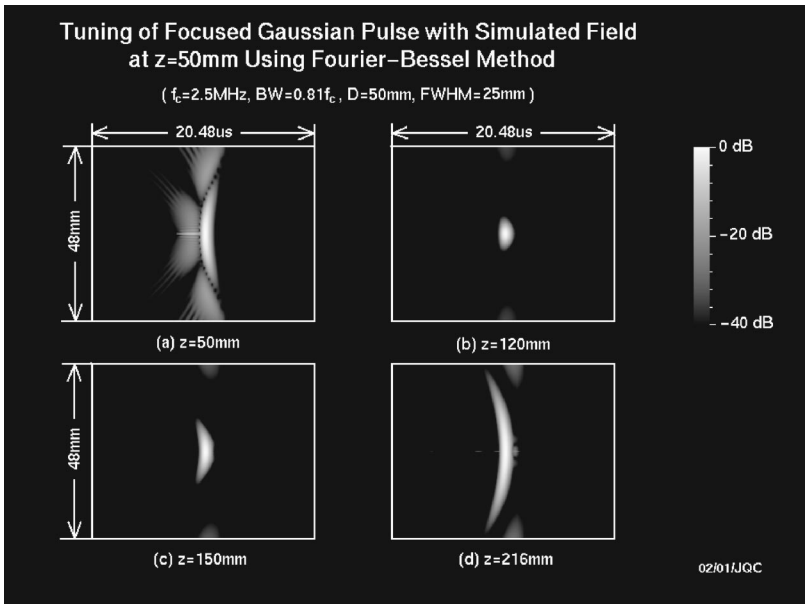

FIG. 8. Tuning results of focused Gaussian pulse with simulated field at $z=50$ mm (Fig. 4(a)) as a desired field using Fourier–Bessel method. With the tuned weighting of the transducer, fields were reconstructed at distances: (a) $z=50$ mm, (b) $z=120$ mm, (c) $z=150$ mm, and (d) $z=216$ mm, respectively, away from the transducer surface.

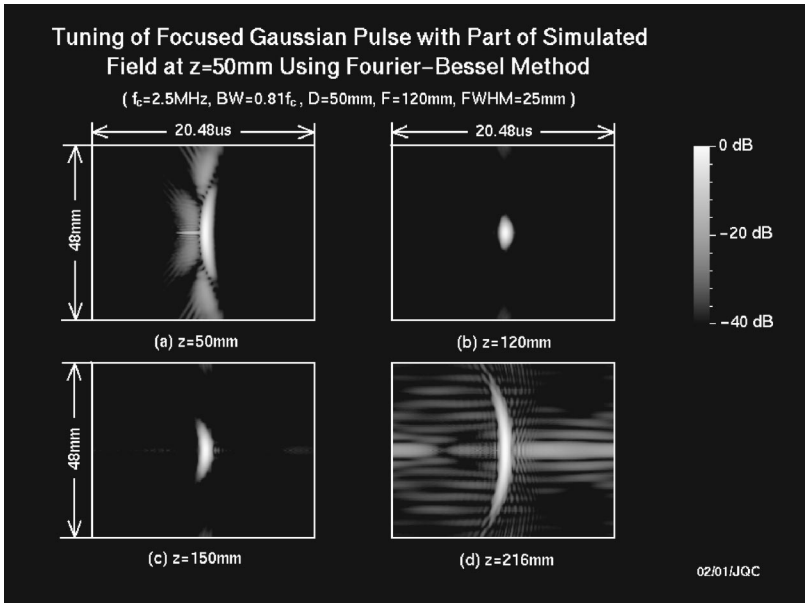

FIG. 9. Tuning results of focused Gaussian pulse with part of the simulated field at $z=50$ mm [Fig. 4(a)] as a desired field using Fourier–Bessel method. Within $r \leqslant 12$ mm, the desired field was the same as the simulated field in Fig. 4(a), otherwise it was set to zero. With the tuned weighting of the transducer, fields were reconstructed at distances: (a) $z=50$ mm, (b) $z=120$ mm, (c) $z=150$ mm, (d) $z=216$ mm.

(10) Reconstruct all quantization levels $Q_p(\omega_s)=\gamma_p(\omega_s)+j\,\delta_p(\omega_s)$ using $\gamma_p(\omega_s)$ and $\delta_p(\omega_s)$ from $T_{ls}(\omega_s)$.
(11) If $s<n_\omega$, increase s by 1 and go back to step (3).
(12) Evaluate time domain quantization values $q_p(t_d)=\mathrm{IFFT}\{Q_p(\omega_s)\}$ from Eq. (5) based on all coefficients $Q_p(\omega_s)$.

VII. EXAMPLES OF TUNING

A. X wave

Now consider tuning the transducer to produce an X wave using the algorithm of Sec. VI B. The intention here is to show that by defining a desired field as an X wave at a given location in space ($z=85$ mm), we are able to tune the transducer quantization levels so as to generate this X wave profile as closely as possible. If this is achievable, it will be evidenced by the pulse created from these quantization levels being essentially identical to the original X wave simulation already shown at the distances (a) $z=85$ mm, (b) $z=170$ mm, (c) $z=255$ mm, (d) $z=340$ mm in Fig. 1. To implement the algorithm we begin with taking the field in Fig. 1(a) as the desired field $d(r,z,t_d)$ and obtain $D(r,z,\omega_s)=\mathrm{FFT}\{d(r,z,t_d)\}$ from Eq. (22) at all sampling points $r=r_u$ of interest; namely those corresponding to a vertical line across the entire diameter of the transducer at an axial distance of $z=85$ mm into the medium. The sampling resolution in the lateral (r) direction is taken as 0.12 mm which complies with the maximum upper bound of $\pi/2k_c=0.15$ mm discussed in Sec. VI. Running the algorithm produces convergence of terms at $a=20R$ and the field resulting from the corresponding tuned transducer quantization levels is shown in Fig. 7 at distances (a) $z=85$ mm, (b) $z=170$ mm, (c) $z=255$ mm, (d) $z=340$ mm. Notice that these are essentially identical to those of Fig. 1, with only some very small differences along the central axis in the far field around $z=340$ mm in panel (d). From the extremely close similarity in propagated pulses for both original and tuned X waves simulations, we may conclude that the tuning algorithm is indeed producing the correct surface pressure profiles required to generate the desired (realizable) pulse in the medium.

B. Focused Gaussian pulses

In Fig. 8 we show the same tuning approach, but this time for the focused Gaussian pulse with desired field as per the simulated field in Fig. 4(a) at $z=50$ mm. Again, the original and regenerated fields at the tuning positions are virtually identical (Figs. 4 and 8, respectively), as are the field shots at the remaining distances (b) $z=120$ mm, (c) $z=150$ mm, (d) $z=216$ mm. This again demonstrates correct tuning of the quantization levels, but this time to produce the focused Gaussian pulse. Figure 9 shows the results once again for a focused Gaussian beam, but this time based on an adaption of the field given in Fig. 4(a). The adaption is to set the desired field at $z=50$ mm to zero beyond $r=12$ mm, which is to say a truncation of the original Gaussian profile in the radial direction. Feeding this new desired field into the tuning algorithm then gives propagating field as per panels (a)–(d) in Fig. 9. Figure 9(a) in this case remains very similar to Fig. 4(a), showing that requiring the field beyond $r=12$ mm being zero whilst at the same time keeping the

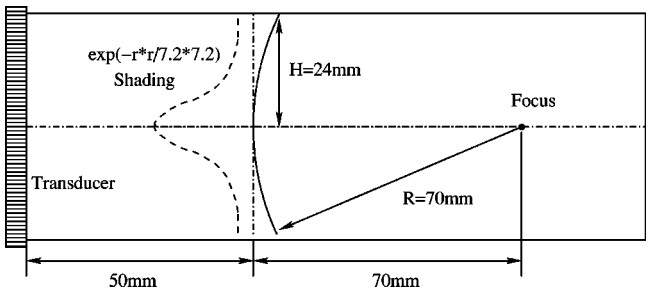

FIG. 10. Schematic diagram of an arbitrarily designed focused pulse. The pulse is 50 mm away from the transducer surface. The shape of pulse in axial direction is an arc with a height and radius of 24 and 70 mm, respectively. The weighting of the pulse in lateral (r) direction is a Gaussian function with $\sigma=7.2$ mm (FWHM=12 mm).

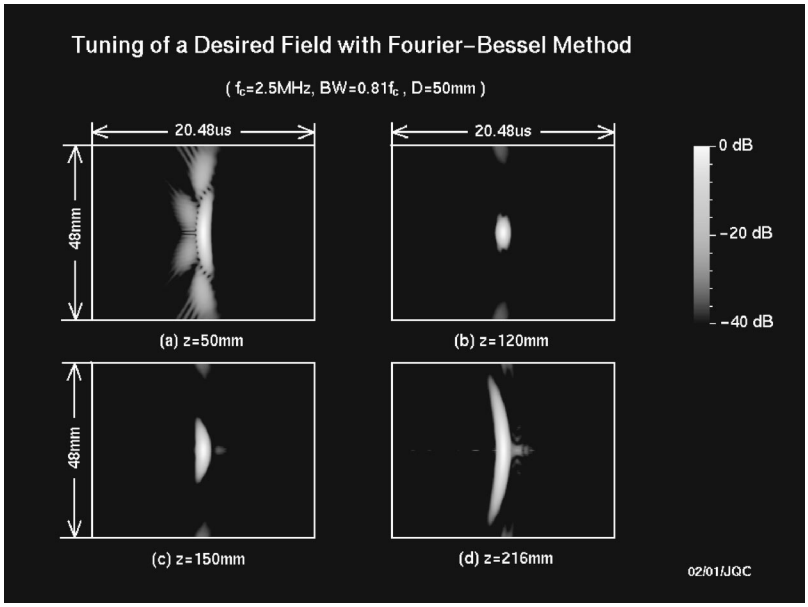

FIG. 11. Tuning results with a designed focused field at $z=50$ mm in Fig. 10 using Fourier–Bessel method. With the tuned weighting of the transducer, fields were reconstructed at distances: (a) $z=50$ mm, (b) $z=120$ mm, (c) $z=150$ mm, and (d) $z=216$ mm, respectively.

original field segment for $0 \leqslant r \leqslant 12$ mm cannot in fact be achieved. Furthermore, the attempt to attain the truncated field distribution at $z=50$ mm not only proves impossible but also leads to a considerable distortion at $z=216$ mm with respect to the original field. Therefore this example illustrates the important point that not all desired fields are achievable, merely that the algorithm tunes the field in a least-squares sense with respect to a given desired field. Hence the topic of which desired fields are realizable and which are not is one which needs further attention in future work.

To illustrate a more successful attempt, Fig. 10 then gives a schematic diagram of an alternative desired focused Gaussian pulse. The pulse is depicted as it passes through the vertical (radial) line at $z=50$ mm away from the transducer surface. The shape of the pulse in the axial direction is an arc with a height and radius of 24 and 70 mm, respectively, with the intended focus being at $z=50+70=120$ mm. The shading in the lateral direction is chosen as a Gaussian function with σ in Eq. (21) now taken as $\sigma=7.2$ mm rather than $\sigma=15$ mm previously. This selection causes the amplitude to reduce to half at $r=6$ mm, thus FWHM$=12$ mm as compared to 25 mm previously. The pulse wave front travels at a velocity $c=1500\ \mathrm{m\,s^{-1}}$ and the corresponding projection of the wave front along the radial r axis as it travels through $z=50$ mm gives the desired field $d(r,z,t)$ for the tuning algorithm. Figure 11 then gives the tuned field results at (a) $z=50$ mm, (b) $z=120$ mm, (c) $z=150$ mm, (d) $z=216$ mm. Figure 11(b) shows that the pulse focuses at $z=120$ mm as intended, and the fields in Figs. 11(a), (c), and (d) then demonstrate broadly the same propagation characteristics before and after focus as for the original Gaussian pulse considered in Fig. 4. Hence this example demonstrates a case where the desired field is actually realisable to within a satisfactory degree, in contrast to that discussed earlier in Fig. 9.

VIII. CONCLUSIONS AND FURTHER WORK

A method has been given for computing and tuning the linear lossless field of flat PW annular arrays using 1D Fourier–Bessel series. The series corresponds to a set of known Bessel beams propagating into the medium, which provides a linear mapping between the transducer surface and the field at any point in space. The method was found to be computationally fast whilst maintaining accuracy and offering computation arbitrarily close to the transducer surface. The related tuning method derived then enabled beamforming of the propagated field in a least-squares sense with respect to a given desired field. However, further work is still needed to determine which desired fields are realisable for a given transducer geometry.

Other possible developments of the current work are also evident. First, an extension to lossy media is of interest in order to model propagation in a wider set of media such as human tissue. Second, an extension to a Bessel-based technique for nonlinear propagation would useful if such progress could be made. Third, its extension to an analysis of two-dimensional (2D) arrays is of prime interest. This would require the use of 2D Fourier–Bessel series, which are capable of modeling non-circular-symmetric quantization profiles and thereby more generalized field distributions. However, whilst conceptually a straightforward progression, the use of 2D series will necessarily lead to higher computational demands due to the increased number of Bessel terms and transducer elements involved.

ACKNOWLEDGMENTS

This work was supported partially by Grant No. HL 60301 from the National Institutes of Health, USA, and No. 26-01-0178 from the Danish Science Foundation, Denmark.

[1] G. Tolstov, *Fourier Series* (Dover, New York, 1962).
[2] F. Bowman, *Introduction to Bessel Functions* (Dover, New York, 1958).
[3] J. A. Stratton, *Electromagnetic Theory* (McGraw–Hill, New York, 1941), p. 356.
[4] J. Durnin, "Exact solutions for nondiffracting beams. I. The scalar theory," J. Opt. Soc. Am. A **4**, 651–654 (1987).
[5] J.-Y. Lu and J. F. Greenleaf, "Nondiffracting X waves—Exact solutions to free-space scalar wave equation and their finite aperture realizations," IEEE Trans. Ultrason. Ferroelectr. Freq. Control **39**, 19–31 (1992).
[6] J.-Y. Lu and J. F. Greenleaf, "Ultrasonic nondiffracting transducer for

medical imaging,'' IEEE Trans. Ultrason. Ferroelectr. Freq. Control **37**, 438–447 (1990).
[7] P. R. Stepanishen and J. Sun, ''Acoustic bullets: Transient Bessel beams generated by planar apertures,'' J. Acoust. Soc. Am. **102**, 3308–3318 (1997).
[8] S. Holm, ''Bessel and conical beams and approximation with annular arrays,'' IEEE Trans. Ultrason. Ferroelectr. Freq. Control **45**, 712–718 (1998).
[9] P. R. Stepanishen, ''Acoustic bullets/transient Bessel beams: Near to far field transition via an impulse response approach,'' J. Acoust. Soc. Am. **103**, 1742–1751 (1998).
[10] P. R. Stepanishen, ''A generalized modal impulse response and Fourier transform approach to investigate acoustic transient Bessel beams and Bessel bullets,'' J. Acoust. Soc. Am. **105**, 1493–1502 (1999).
[11] J.-Y. Lu and A. Liu, ''An X wave transform,'' IEEE Trans. Ultrason. Ferroelectr. Freq. Control **47**, 1472–1481 (2000).
[12] P. D. Fox and S. Holm, ''Modelling of CW annular arrays using limited diffraction Bessel beams,'' IEEE Trans. Ultrason. Ferroelectr. Freq. Control **49**, 85–93 (2002).
[13] P. D. Fox, J. Cheng, and J.-Y. Lu, ''Fourier-bessel field calculation and tuning of a CW annular array,'' IEEE Trans. Ultrason. Ferroelectr. Freq. Control **49**, 1179–1190 (2002).
[14] J. H. Mcleod, ''The Axicon: A new type of optical element,'' J. Opt. Soc. Am. **44**, 592 (1954).
[15] C. B. Burckhardt, H. Hoffmann, and P. A. Grandchamp, ''Ultrasound axicon: A device for focusing over a large depth,'' J. Acoust. Soc. Am. **54**, 1628–1630 (1973).
[16] J. Fagerholm, A. T. Friberg, J. Huttunen, D. P. Morgan, and M. M. Salomaa, ''Angular-spectrum representation of nondiffracting X waves,'' Phys. Rev. E **54**, 4347–4352 (1996).
[17] K. Uehara and H. Kikuchi, ''Generation of near diffraction-free laser beams,'' Appl. Phys. B: Photophys. Laser Chem. **48**, 125–129 (1989).
[18] A. Vasara, J. Turunen, and A. T. Friberg, ''Realization of general nondiffracting beams with computer-generated holograms,'' J. Opt. Soc. Am. A **6**, 1748–1754 (1989).
[19] J. N. Brittingham, ''Focus wave modes in homogeneous Maxwell's equations: Transverse electric mode,'' J. Appl. Phys. **54**, 1179–1189 (1983).
[20] R. W. Ziolkowski, ''Exact solutions of the wave equation with complex source locations,'' J. Math. Phys. **26**, 861–863 (1985).
[21] R. W. Ziolkowski, D. K. Lewis, and B. D. Cook, ''Evidence of localized wave transmission,'' Phys. Rev. Lett. **62**, 147–150 (1985).
[22] J.-Y. Lu and J. F. Greenleaf, ''Pulse-echo imaging using a nondiffracting beam transducer,'' Ultrasound Med. Biol. **17**, 265–281 (1991).
[23] J.-Y. Lu, H. Zou, and J. F. Greenleaf, ''Biomedical ultrasound beam forming,'' Ultrasound Med. Biol. **20**, 403–428 (1994).
[24] J.-Y. Lu, ''2D and 3D high frame rate imaging with limited diffraction beams,'' IEEE Trans. Ultrason. Ferroelectr. Freq. Control **44**, 839–856 (1997).
[25] J.-Y. Lu and J. F. Greenleaf, ''Evaluation of a nondiffracting transducer for tissue characterization,'' IEEE 1990 Ultrasonics Symposium Proceedings 90CH2938-9, 1990, Vol. 2, pp. 795–798.
[26] J.-Y. Lu, X.-L. Xu, H. Zou, and J. F. Greenleaf, ''Application of Bessel beam for Doppler velocity estimation,'' IEEE Trans. Ultrason. Ferroelectr. Freq. Control **42**, 649–662 (1995).
[27] J.-Y. Lu and J. F. Greenleaf, ''Producing deep depth of field and depth-independent resolution in NDE with limited diffraction beams,'' Ultrason. Imaging **15**, 134–149 (1993).
[28] J.-Y. Lu and S. He, ''Optical X waves communications,'' Opt. Commun. **161**, 187–192 (1999).
[29] J. Ojeda-Castaneda and A. Noyola-lglesias, ''Nondiffracting wavefields in grin and free-space,'' Microwave Opt. Technol. Lett. **3**, 430–433 (1990).
[30] J. Durnin, J. J. Miceli, Jr., and J. H. Eberly, ''Diffraction-free beams,'' Phys. Rev. Lett. **58**, 1499–1501 (1987).
[31] S. Holm and P. D. Fox, ''Analysis of Bessel beam quantisation in annular arrays,'' Proceedings of the 22nd Scandinavian Symposium on Physical Acoustics, 1999, pp. 43, 44, Ustaoset, Norway, ISSN 1501–6773.
[32] P. D. Fox and S. Holm, ''Decomposition of acoustic fields in quantised Bessel beams,'' Ultrasonics **38**, 190–194 (2000).
[33] J.-Y. Lu and J. F. Greenleaf, ''Experimental verification of nondiffracting X waves,'' IEEE Trans. Ultrason. Ferroelectr. Freq. Control **39**, 441–446 (1992).
[34] G. E. Tupholme, ''Generation of acoustic pulses by baffled plane pistons,'' Mathematika **16**, 209–224 (1969).
[35] P. R. Stepanishen, ''The time-dependent force and radiation impedance on a piston in a rigid infinite planar baffle,'' J. Acoust. Soc. Am. **49**, 841–849 (1971).
[36] P. R. Stepanishen, ''Acoustic transients from planar axisymmetric vibrators using the impulse response approach,'' J. Acoust. Soc. Am. **70**, 1176–1181 (1981).
[37] M. Arditi, F. S. Forster, and J. Hunt, ''Transient fields of concave annular arrays,'' **3**, 37–61 (1981).
[38] J. A. Jensen, ''Field: A program for simulating ultrasound systems,'' MBEC 10th Nordic-Baltic Conference on Biomedical Imaging, 1996, Vol. 4, Supplement 1, Part 1, pp. 351–353.
[39] J. A. Jensen, ''A new calculation procedure for spatial impulse responses in ultrasound,'' J. Acoust. Soc. Am. **105**, 3266–3274 (1999).